Available online at www.sciencedirect.com
SCIENCE DIRECT®
Journal of Solid State Chemistry 178 (2005) 285–294
JOURNAL OF SOLID STATE CHEMISTRY
www.elsevier.com/locate/jssc

Trends in negative thermal expansion behavior for AMO_2 (A = Cu or Ag; M = Al, Sc, In, or La) compounds with the delafossite structure

J. Li[a], A.W. Sleight[a,*], C.Y. Jones[b], B.H. Toby[b]

[a]*Department of Chemistry, Oregon State University, Room 153, Gilbert Hall, Corvallis, OR 97331-4003, USA*
[b]*NIST Center for Neutron Research, National Institute of Standards and Technology, 100 Bureau Drive, Stop 8562, Gaithersburg, MD 20899-8562, USA*

Received 1 September 2004; received in revised form 4 November 2004; accepted 11 November 2004

Abstract

Powder neutron diffraction data were obtained from 30 to 600 K for $CuAlO_2$, $CuInO_2$, $CuLaO_2$, 2H $CuScO_2$, 3R $CuScO_2$, and $AgInO_2$. Rietveld refinements of these data showed negative thermal expansion (NTE) of the O–Cu–O linkage in all cases. This behavior was especially strong for $CuLaO_2$ and $CuScO_2$, where it persisted up to our maximum measuring temperature of 600 K. This NTE in turn caused NTE of the c cell edge, which was moderated by the positive thermal expansion of the M–O bonds. The NTE behavior increases in the $CuMO_2$ series as the size of M increases. No NTE behavior was found for the O–Ag–O linkage in $AgInO_2$; nonetheless, this compound did exhibit NTE for the c cell edge at low temperatures. For $CuLaO_2$ there is NTE for both the a and c cell edges at low temperatures. Structural trends for compounds with the delafossite structure are discussed with respect to both composition and temperature.

Keywords: Delafossite structure; Negative thermal expansion; Powder neutron diffraction

1. Introduction

Strong negative thermal expansion (NTE) has now been established for many oxides with network structures having oxygen in two-fold coordination [1]. The NTE behavior in these cases is caused by the thermal motion of oxygen transverse to M–O–M linkages. The exceptionally large NTE behavior found for $Zn(CN)_2$ is presumably also related to transverse thermal motion of C and N in the Zn–C–N–Zn linkage [2]. There is apparently just one known example of NTE behavior in an oxide where the oxygen coordination is three. This is Zn_2SiO_4 where all oxygen atoms are three coordinated in an arrangement very close to planar [3]. This NTE behavior is presumably caused by oxygen thermal motion perpendicular to the plane of the three cations to which oxygen is bonded. This mechanism for NTE would then be analogous to the situation in graphite. Carbon is three coordinated, and thermal motion perpendicular to the strong bonds in the sheets results in NTE behavior for the a and b cell edges. The distance between the sheets increases with increasing temperature, leading to strong positive thermal expansion along the c-axis.

The thermal expansion behavior of several compounds isostructural with Zn_2SiO_4 has been studied; some show low thermal expansion, but none show any NTE behavior [4]. NTE behavior is also known in $PbTiO_3$, where the behavior is driven by the polyhedra becoming more regular with increasing temperature [1]. NTE behavior has also been observed in nonoxide materials such as $Sm_{0.75}Y_{0.25}S$ [5] and YbGaGe [6].

NTE behavior can also occur in oxides where the cation is in two-fold coordination. This coordination is rare, and the only two cations that are known to support

*Corresponding author. Fax: +1 541 737 2062.
E-mail address: arthur.sleight@orst.edu (A.W. Sleight).

0022-4596/$ - see front matter
doi:10.1016/j.jssc.2004.11.017

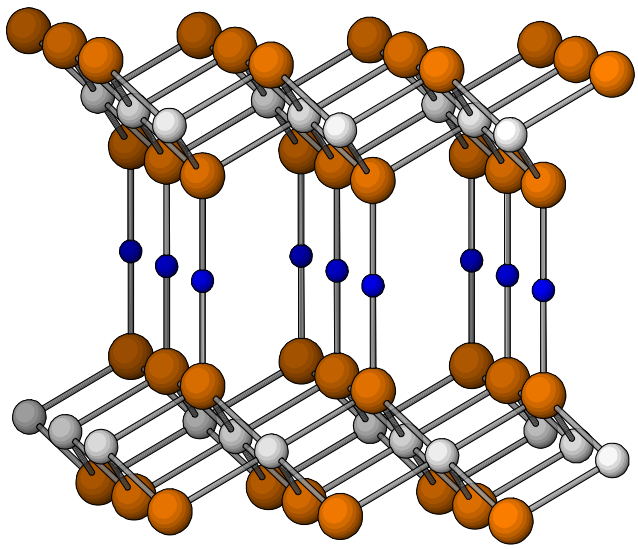

Fig. 1. A fragment of the 3R AMO_2 delafossite structure with the c-axis vertical where small atoms are A (A = Ag, Cu), medium atoms are M (M = La, In, Sc, Al), and large atoms are O. The 3R and 2H forms differ by stacking along the c-axis: ABC stacking for 3R and ABAB for 2H.

two-fold coordination and NTE behavior are Cu(I) and Ag(I). The same cubic structure is found for Cu_2O and Ag_2O, and both compounds exhibit NTE behavior [7]. Compounds with the AMO_2 formula having the delafossite structure (Fig. 1) have two-fold coordination for the A cation, which can be Cu(I) or Ag(I). We have previously shown that 2H $CuScO_2$ with the delafossite structure shows NTE behavior for the c cell edge below room temperature [8]. The purpose of this paper is to compare the thermal expansion in the delafossite structure as the M and A cations are varied. Besides our study of 2H $CuScO_2$, there is only one publication on structure variation with temperature of a compound with delafossite structure. This is for $CuAlO_2$, where the temperature range was 295–1200 K [9]. No NTE behavior was observed over that temperature range.

2. Experimental

2.1. Synthesis

Reagents used were Cu_2O (Cerac, 99%), La_2O_3 (Aldrich, 99.99%), Al_2O_3 (Aldrich, 99.8%), Sc_2O_3 (Stanford Materials, 99.99%), CuCl (Alfa Aesar, 99%), Li_2CO_3 (Sigma, 99.6%), MgO (Aldrich, 99%), In_2O_3 (Cerac, 99.99%), Na_2CO_3 (Aldrich, 99.99%), $AgNO_3$ (Spectrum, 99.0%) and KOH (Mallinckrodt, AR). Samples of CuCl obtained from several manufacturers were all badly contaminated with Cu(II) oxyhydroxide. This impurity was removed by washing with dilute hydrochloric acid.

The $CuLaO_2$ sample was synthesized by the solid-state reaction of Cu_2O and La_2O_3 following the method of Cava et al. [10]. Freshly calcined La_2O_3 (1000 °C, air, overnight) was mixed with Cu_2O in a stoichiometric ratio, ground in an agate mortar, and pressed into pellets. These pellets were buried in powders of the same composition in an alumina crucible, covered, and heated in an argon flow at 1000 °C for 24 h.

The $CuAlO_2$ sample was prepared by a solid-state reaction in air. Equimolar amounts of Cu_2O and Al_2O_3 were mixed by grinding in an agate mortar and pressed into pellets. These pellets were heated at 1100 °C for 24 h and quench cooled in air.

Our synthesis methods for 2H and 3R $CuScO_2$ samples have previously been reported [8,11]. To prepare the pure 2H sample free of the 3R form 5% Mg is substituted for Sc.

The $CuInO_2$ sample was prepared by an ion-exchange reaction similar to that of 3R $CuScO_2$ [11]. Equimolar amounts of Na_2CO_3 and In_2O_3 were mixed and heated at 1000 °C in air for 12 h. The $NaInO_2$ powder obtained was mixed with purified CuCl in a molar ratio of 1:1.3, and the mixture was placed in a Cu crucible inside a stainless steel vessel with Ar flowing through. The vessel was then heated to 550 °C for 6 h. The reaction product was washed with 2 M aqueous NH_4OH to remove NaCl and excess CuCl. The final product was dried in air.

The polycrystalline sample of $AgInO_2$ was synthesized by a hydrothermal reaction. Stoichiometric amounts of $AgNO_3$ and In_2O_3 in 5 M KOH aqueous solution were sealed in a PTFE autoclave within a Parr bomb. The reaction was carried out at 250 °C for 7 days. The resulting orange highly crystalline $AgInO_2$ was washed with distilled water to remove the adsorbed KOH/KNO_3 solution.

2.2. Neutron diffraction

Neutron powder diffraction data were collected using the BT-1 32-counter high-resolution diffractometer at the NIST Center for Neutron Research at the National Institute of Standards and Technology. A Cu(311) monochromator with a 90° take-off angle giving a wavelength of 1.5402(2) Å and in-pile collimation of 15 min of arc were used. The beam was masked to 1.1 × 5.1 cm at the sample. Data were collected over a 2θ range of 3–168° with a step size of 0.05° and a temperature range of 30–600 K. Our data for 2H $CuScO_2$ from 11 to 1206 K have been previously reported [8], but are given here again up to 600 K for comparison. In addition, data on 2H $CuScO_2$ was collected at 3.6 K using a Ge(733) monochromator with a takeoff angle of 120° giving a wavelength of 1.1976(2) Å. Additional data were also collected for $CuLaO_2$ at very low temperatures down to 4 K. Samples of 2H and 3R $CuScO_2$ and $AgInO_2$ were sealed in

vanadium containers 15.6 mm in diameter and 50 mm high, and samples of $CuLaO_2$, $CuAlO_2$ and $CuInO_2$ were sealed in vanadium containers 10.8 mm in diameter and 50 mm high. The measurement time for each temperature was 2–3 h. A vacuum furnace was used for measurements above room temperature, and a closed-cycle He refrigerator was used for measurements below room temperature. The data of $CuScO_2$, $CuInO_2$ and $AgInO_2$ were corrected for absorption [12]. All the data were fit by the Rietveld method using GSAS software [13,14].

3. Results

Compounds investigated in this study are $CuAlO_2$, $CuInO_2$, $AgInO_2$, $CuLaO_2$, and $CuScO_2$. All compounds have the 3R form of the delafossite structure, except that in the case of $CuScO_2$ both the 2H and the 3R forms were studied. The 2H structure was refined in space group $P6_3/mmc$ with atom positions of Cu ($\frac{1}{3}, \frac{2}{3}, \frac{1}{4}$), M (0,0,0), and O ($\frac{1}{3}, \frac{2}{3}, z$). The 3R structure was refined in space group $R\bar{3}m$ with hexagonal atom positions of Cu or Ag (0,0,0), M (0,0,$\frac{1}{2}$), and O (0,0,z). This study encompasses results from 49 different refinements. Due to space limitations, results are only presented here graphically. However, all agreement factors, atomic coordinates, thermal displacement factors, and interatomic distances are available in the CIF files. The absence of interstitial oxygen was confirmed by placing oxygen in the Cu triangles within the Cu planes. The occupancy of such sites always refined to values indistinguishable from zero.

Figs. 2 and 3 show the a and c cell edge variations with temperature. NTE behavior was observed at low temperature for all compounds investigated. Usually the NTE behavior was just for the c cell edge. The low temperature value of α was -1.0 to -1.8×10^{-6}/K in most cases but was only -0.4 and -0.5×10^{-6}/K for $CuAlO_2$ and $CuInO_2$, which makes the NTE effect difficult to see in Fig. 3. In the case of $CuLaO_2$ NTE behavior was found for both a and c. In no case was there NTE behavior for any cell edge above room temperature. In Fig. 4 the c/a ratio is plotted against temperature. This indicates that the thermal expansion is generally highly anisotropic, which is expected for such an anisotropic structure. However, nearly isotropic thermal expansion is found in the case of $CuLaO_2$.

The term atomic displacement factor has generally replaced the term thermal parameter because atomic displacements are not always thermally induced. We use the term thermal parameter here because the temperature dependences of these terms indicate they are basically true thermal parameters. Figs. 5–7 show the variations of thermal parameters with temperature. All atoms are on a three-fold axis. Thus, the thermal

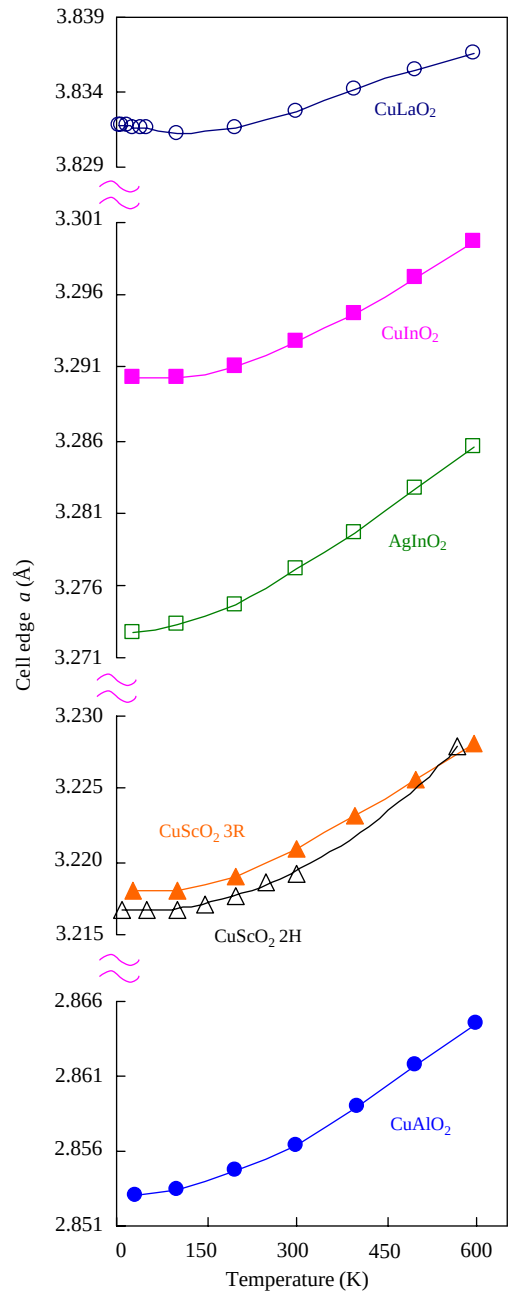

Fig. 2. The a cell edges vs. temperature.

ellipsoids are either extended or flattened along this axis. U_{11} is perpendicular to the c-axis, and U_{33} is parallel to the c-axis. The most extreme anisotropic Us are for the A cation. As expected for two-fold linear coordination, the ellipsoids are flattened, and the U_{11}/U_{33} ratio can be four or higher. The opposite situation is generally found for the M cations. The ellipsoids are usually elongated along the c-axis. Anisotropic thermal motion would not be expected in a regular octahedron, but this octahedron is highly distorted. The more pronounced motion is in the direction of the two faces that are much larger than the other four faces. The main exception is found for

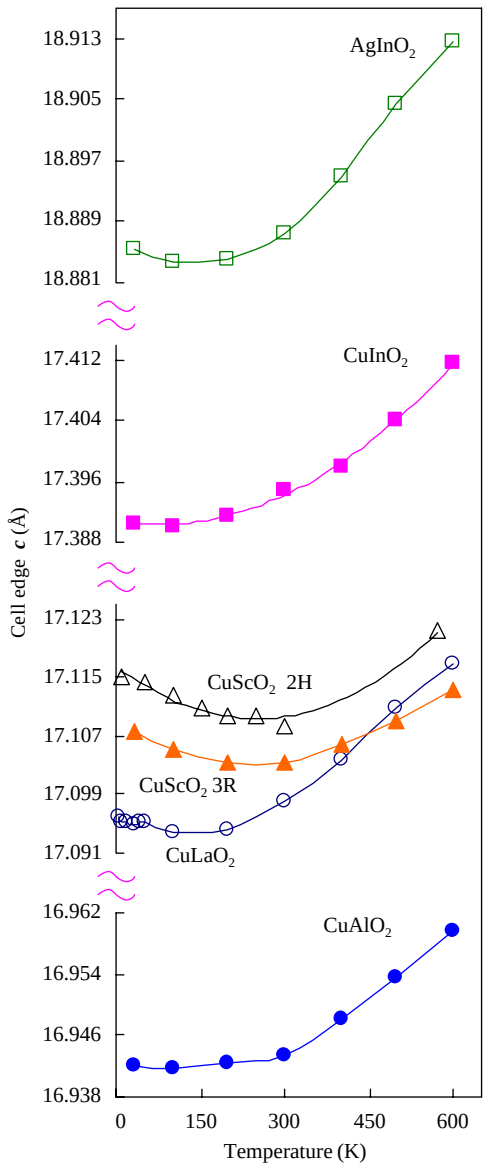

Fig. 3. The c cell edges vs. temperature. The values for 2H $CuScO_2$ have been multiplied by $\frac{3}{2}$ to allow direct comparison.

$CuInO_2$, where the distortion from a regular octahedron is not so great. Here thermal motion of oxygen is nearly isotropic, but there is a tendency of U_{11} to be somewhat higher than that of U_{33}. The standard uncertainties for U values vary from about the same size of the points ($CuLaO_2$) to about twice of the size of the points ($CuInO_2$) in Figs. 5–7. It is physically unreasonable for U_{11} or U_{33} to be negative, and these values were found to be positive for all atoms in all compounds at room temperature. However, some of these parameters did sometimes minimize to negative values at low temperatures, usually within a few standard uncertainties of zero. Applying corrections for absorption did not always rectify this. The lower range of these values is attributed to correlation between the U values and other fitted values, likely the background parameters. This

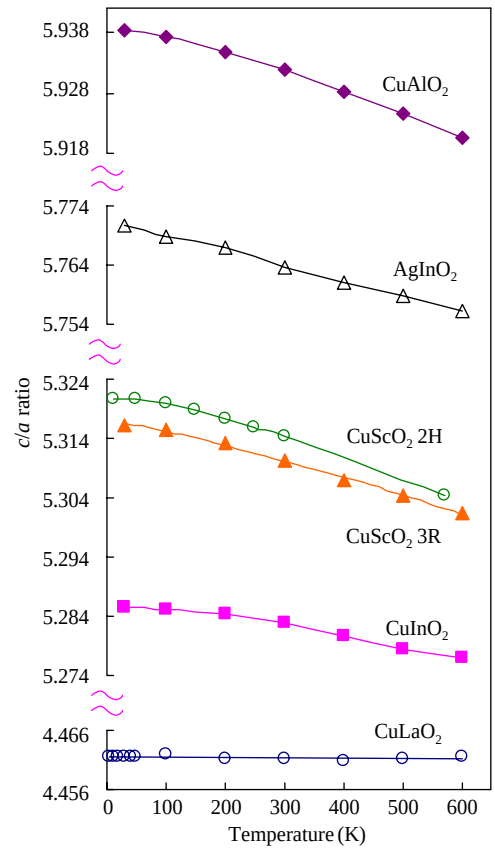

Fig. 4. Cell edge c/a ratio vs. temperature.

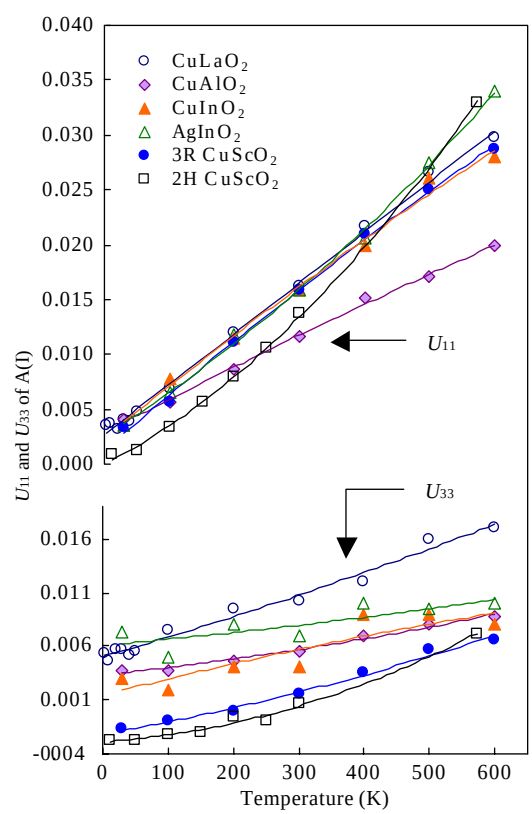

Fig. 5. Thermal displacement factors of A(I) cation (A = Cu, Ag) vs. temperature.

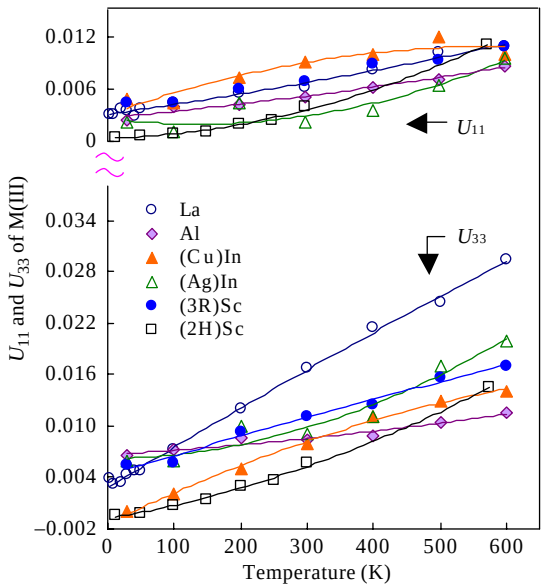

Fig. 6. Thermal displacement factors of M(III) (M = La, In, Sc, Al) vs. temperature.

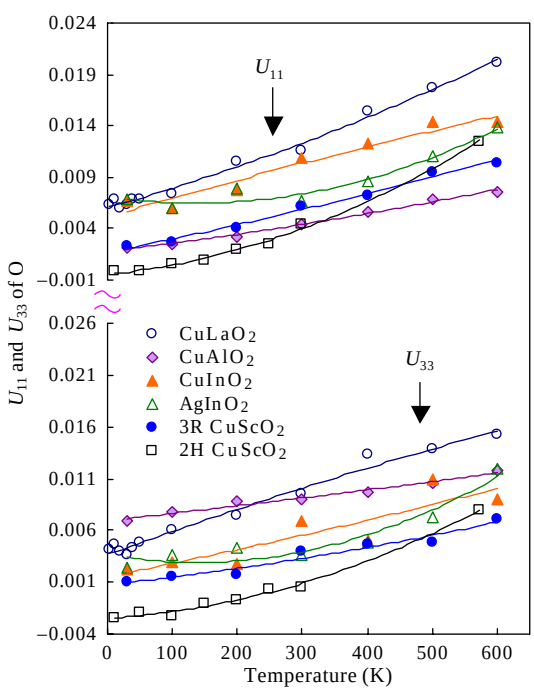

Fig. 7. Thermal displacement factors of oxygen vs. temperature.

conclusion was supported by collecting data for 2H $CuScO_2$ at 3.6 K using a shorter neutron wavelength. This approximately doubles the number of accessible reflections, which increases the sensitivity of the fit to the thermal parameters. With this greater range of data, all U parameters refined to positive values or zero.

Fig. 8 plots our data for Cu U_{11} in $CuAlO_2$, together with the data from the previous single crystal X-ray study [9]. The agreement in the overlap area is very

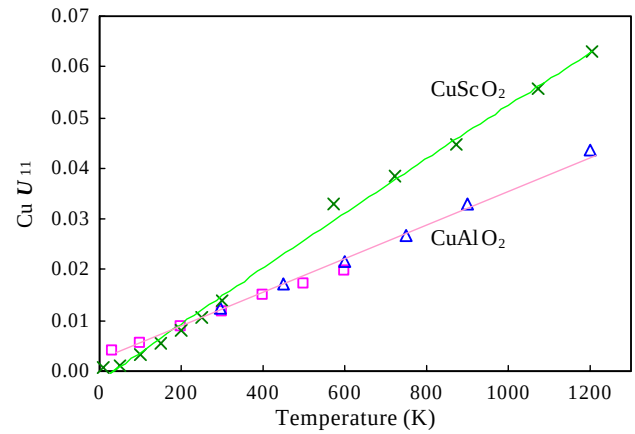

Fig. 8. Comparison of thermal displacement factors of Cu U_{11}. Squares (this work, powder neutron diffraction) and triangles ([9], single crystal XRD) are for 3R $CuAlO_2$. Cross points are for 2H $CuScO_2$ ([8], powder neutron diffraction).

good. Our Cu U_{11} data for 2H $CuScO_2$ are also plotted for comparison, showing that Cu(I) maintains a larger thermal motion perpendicular to the c-axis in 2H $CuScO_2$ than in $CuAlO_2$ up to high temperatures.

The variations of the uncorrected and corrected A–O distances with temperature are shown in Fig. 9, indicating that strong NTE behavior persists in some cases up to our maximum measuring temperature of 600 K. The M–O distances vs. temperature are in Fig. 10, and the thicknesses of the $(MO_2)^{1-}$ layers as a function of temperature are shown in Fig. 11. Due to the high symmetry of this structure, the A–A distance, the M–M distance, and one O–O distance are the same as a cell edge.

The values of the cell edges can be determined with greater accuracy than the bond distances. Thus, the estimated errors for a, c, and T are less than the size of the points in the figures. The estimated errors for the values in Figs. 9–11 depend on the accuracy of the determination of the O(z) parameter. Estimated uncertainties for interatomic distances vary with the intensities of the various diffraction patterns giving the following estimates for the strongest pattern ($CuLaO_2$) and the weakest pattern ($CuInO_2$), respectively: 0.0001–0.0003 Å for M–O, 0.0003–0.0007 Å for A–O, and 0.0006–0.0015 Å for the sheet thickness.

4. Discussion

4.1. Trends with composition

Before discussion of trends with temperature, it is important to discuss some trends in the delafossite structure with variations of the A and M cations. It has been previously noted by Jansen that the Cu–O distance in $CuMO_2$ delafossites decreases as the size of M and

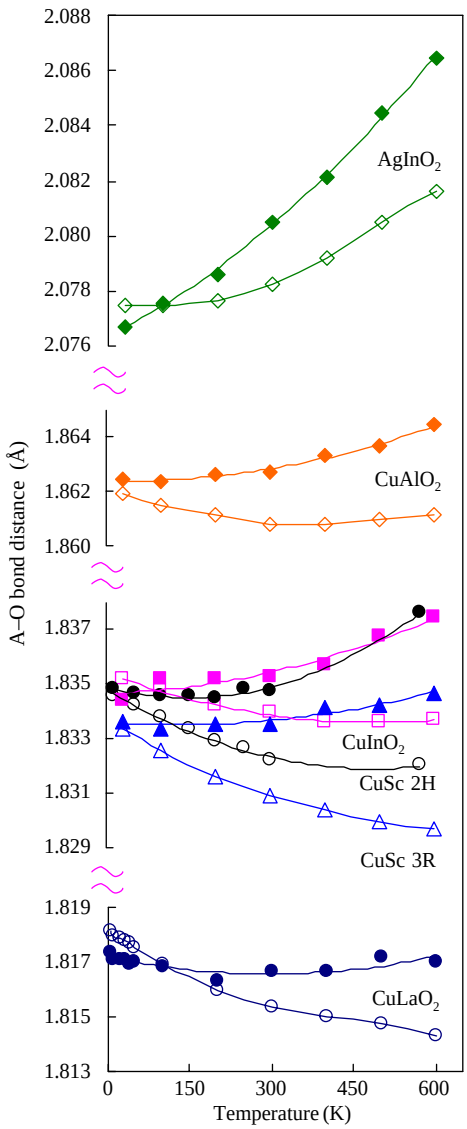

Fig. 9. The temperature dependence of A–O bond distances. Open symbols are uncorrected bond distances. Solid symbols are corresponding bond distances corrected by riding model.

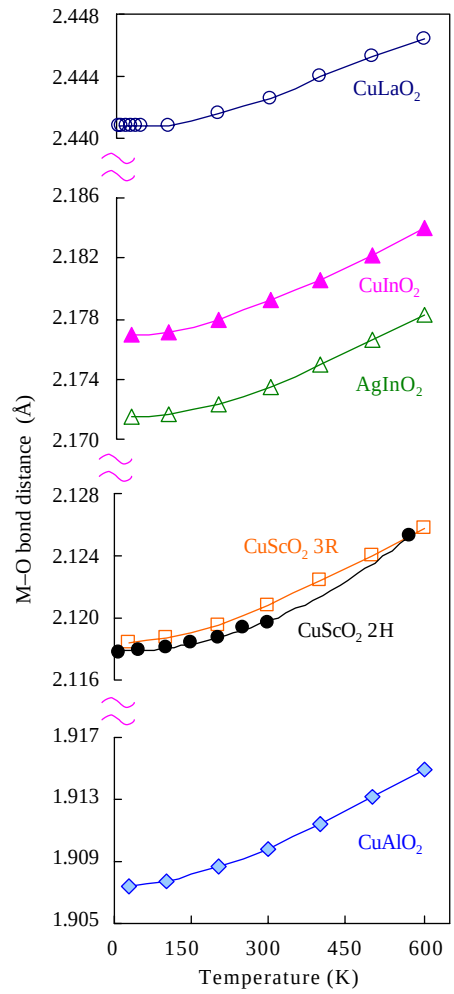

Fig. 10. The M–O bond distances vs. temperature.

consequently the Cu–Cu distance increases [15]. We also note the same trend for the Ag–O distances in AgMO$_2$ delafossites (Fig. 12). Jansen had rationalized this behavior for CuMO$_2$ delafossites on the basis of competition between Cu–O bonding and Cu–Cu bonding. Thus, as one bond becomes shorter and stronger, the other bond becomes longer and weaker. One would not normally expect any bonding interaction between $nd^{10}(n+1)s^0$ cations such as Cu(I) and Ag(I). However, strong d–s hybridization occurs on Cu and Ag due to the linear O–A–O linkages. This effectively transfers some electron density from the filled d shell to the empty s shell. The A–A interaction then becomes weakly bonding, creating an attractive force that is balanced by repulsion between the cores. It is this A–A bonding interaction that presumably provides the conduction mechanism for p-doped CuMO$_2$ compounds with the delafossite structure. However, the A–A bond appears too weak to explain the trend in Fig. 12. We have suggested an alternate explanation [28]. The s–d_z2 hybridization of the A cations necessary to form the two-fold linear bonds to oxygen effectively polarizes the filled shell leading to an increase of the A–A repulsion. As the A cations are forced closer by the smaller M cations, this polarization is forced to decrease, forcing increased antibonding electron density for the A–O bond. Thus, the A–O bond becomes weaker and longer. This explanation was subsequently supported by calculations [27].

Because all the O–A–O linkages are strictly parallel to the c-axis, one expects that the value of the a cell edge will scale only with the size of the M cation. Thus, the magnitudes of the a cell edges for AgMO$_2$ and CuMO$_2$ compounds with the same M cation are nearly the same (Fig. 13). The small differences that do exist in the a cell edges for compounds with the same M cation can give important clues as to the nature of the A–A interaction. For small values of the a cell edge, the AgMO$_2$

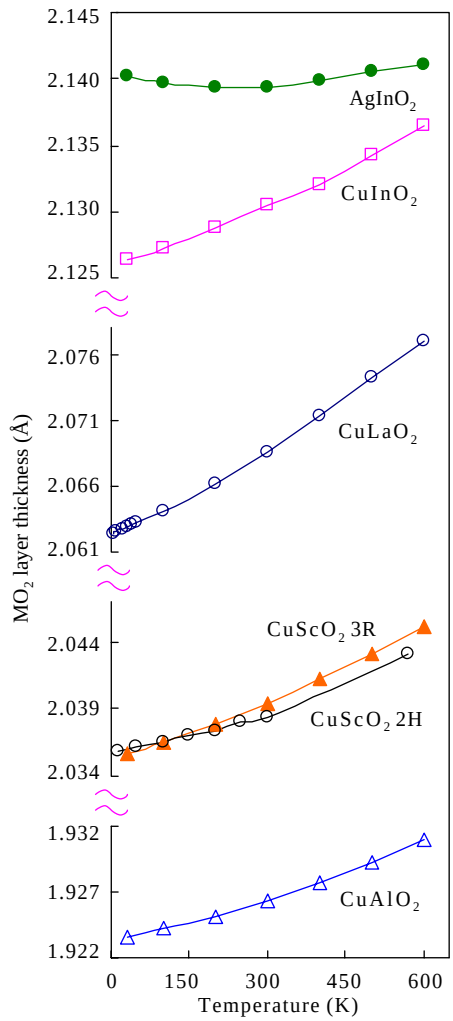

Fig. 11. Thicknesses of the $(MO_2)^{1-}$ layers as a function of temperature.

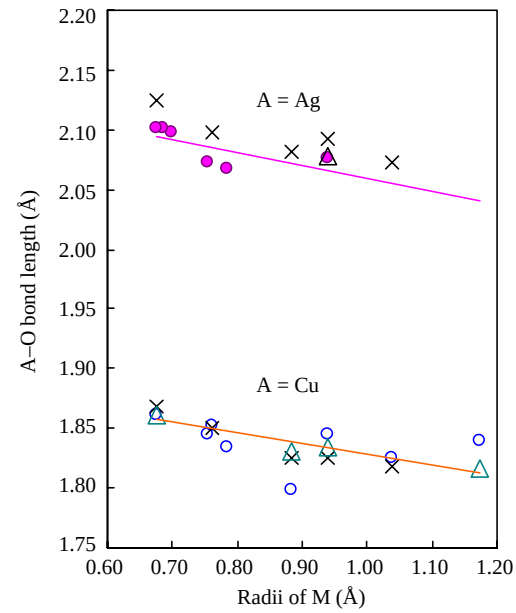

Fig. 12. Variation of A–O bond distances with the size of M cations. Solid circles, from left to right, are for $AgAlO_2$ [16], $AgCoO_2$ [17], $AgNiO_2$ [17], $AgCrO_2$ [18], $AgFeO_2$ [19,20], and $AgInO_2$ [21]. Open circles, from left to right, are for $CuAlO_2$ [9], $CuCrO_2$ [22], $CuGaO_2$ [23], $CuFeO_2$ [19,20], $CuScO_2$ [24], $CuInO_2$ [25], $CuYO_2$ [23], and $CuLaO_2$ [26]. Triangles are data points from this work. Cross points are calculated data (GGA) by Kandpal et al. [27].

compound has a larger a cell edge than does the $CuMO_2$ compound. This can be rationalized on the basis that Ag is larger than Cu, and Ag–Ag repulsive forces will dominate at the smaller A–A distances. The opposite trend occurs at larger A–A distances: the $CuMO_2$ compounds have a larger a cell edge than do the corresponding $AgMO_2$ compounds. This crossover has been predicted from calculations [27]. Such a crossover indicates potential energy curves as shown in Fig. 14. It is assumed that the A–A interaction becomes attractive at large A–A distances, but a crossover could also be consistent with the A–A interaction being repulsive at all distances.

The length of the c cell edge is influenced by both the A–O distance and the M–O distance. If the Cu–O and Ag–O distances remained constant, one would expect a significant increase in the c cell edge as the size of M increases. However as noted above, the A–O distances actually decrease as the size of M increases (Fig. 12). Thus, changes of the A–O and M–O distances as M is varied tend to compensate. The slightly larger increase in the size of the c cell edge with increasing M size for $AgMO_2$ compounds (Fig. 15) relative to $CuMO_2$ compounds is related to the crossover of the a cell edge of $CuMO_2$ and $AgMO_2$ compounds (Fig. 13). The a cell edge does not increase as rapidly with M size for $AgMO_2$ compounds as it does for $CuMO_2$ compounds. Thus, this increase in the size of M has a more pronounced impact on the c cell edge for the $AgMO_2$ compounds.

One must also consider the impact of cation–cation repulsion across the edge-shared octahedra of the $(MO_2)^{1-}$ sheets. This repulsion will increase with the real charge on the M(III) cations and will thus increase as the M(III) cations become more electropositive. The lowest repulsion among M(III) cations we have studied is expected for In, because In has the highest electronegativity. Thus, for $CuInO_2$ and $AgInO_2$ the $(MO_2)^{1-}$ sheets are less stretched and are therefore thicker (Fig. 11), causing a larger c cell edge than would be otherwise expected (Figs. 3 and 15).

The differences between $CuInO_2$ and $AgInO_2$ are also interesting. The Ag–O bond being weaker than the Cu–O bond causes the In–O bond to be stronger and shorter in $AgInO_2$ than in $CuInO_2$ (Fig. 10). This in turn results in the a cell edge for $AgInO_2$ being smaller than for $CuInO_2$ (Fig. 2).

A curious feature of the delafossite structure is that the M–O–M angle is constrained by space group

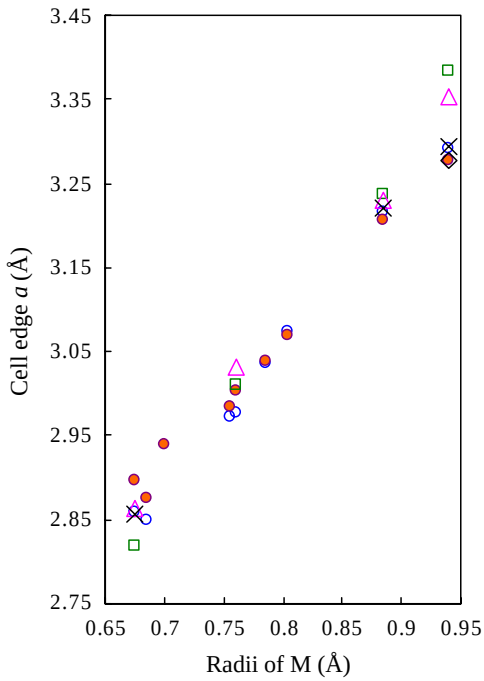

Fig. 13. Variation of cell edge a with the size of M cations. Solid circles, from left to right, are for $AgAlO_2$ [16], $AgCoO_2$ [17], $AgNiO_2$ [17], $AgCrO_2$ [18], $AgGaO_2$ [24], $AgFeO_2$ [19,20], $AgRhO_2$ [19], $AgScO_2$ [28] and $AgInO_2$ [21]. Open circles, from left to right, are for $CuAlO_2$ [9], $CuCoO_2$ [19], $CuCrO_2$ [22], $CuGaO_2$ [23], $CuFeO_2$ [19,20], $CuRhO_2$ [19], $CuScO_2$ [24], and $CuInO_2$ [25]. The diamond is for $AgInO_2$ (this work), and cross points are for $CuMO_2$ (this work). Triangles are calculated (GGA) data for $AgMO_2$ and squares are calculated (GGA) data for $CuMO_2$ [27].

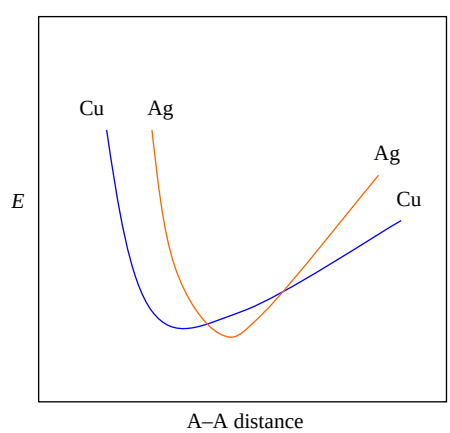

Fig. 14. Schematic of potential energy vs. $A-A$ distance (A = Ag, Cu).

symmetry to be exactly the same as one of the two O–M–O angles. (The sum of the two O–M–O angles is 180°). This angle is plotted vs. the size of M(III) in Fig. 16. Oxygen is tetrahedrally coordinated ($A+3M$), and M is octahedrally coordinated. It is impossible for the M–O–M and O–M–O angles plotted in Fig. 16 to have the ideal values of 109° and 90°. Thus, this angle is

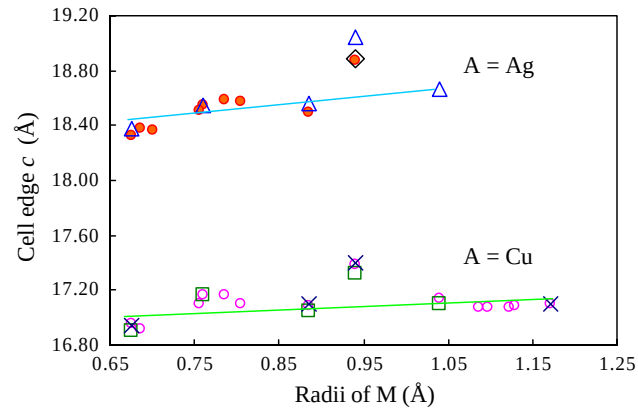

Fig. 15. Variation of cell edge c with the size of M cations. Solid circles, from left to right, are for $AgAlO_2$ [16], $AgCoO_2$ [17], $AgNiO_2$ [17], $AgCrO_2$ [18], $AgGaO_2$ [24], $AgFeO_2$ [19,20], $AgRhO_2$ [19], $AgScO_2$ [28] and $AgInO_2$ [21]. Open circles, from left to right, are for $CuAlO_2$ [9], $CuCoO_2$ [19], $CuCrO_2$ [22], $CuGaO_2$ [23], $CuFeO_2$ [19,20], $CuRhO_2$ [19], $CuScO_2$ [24], $CuInO_2$ [25], $CuYO_2$ [23], $CuEuO_2$ [26], $CuSmO_2$ [26], $CuNdO_2$ [29], $CuPrO_2$ [26], $CuLaO_2$ [26]. The diamond is for $AgInO_2$ (this work), and cross points are for $CuMO_2$ (this work). Triangles are calculated (GGA) data for $AgMO_2$ and squares are calculated (GGA) data for $CuMO_2$ [27].

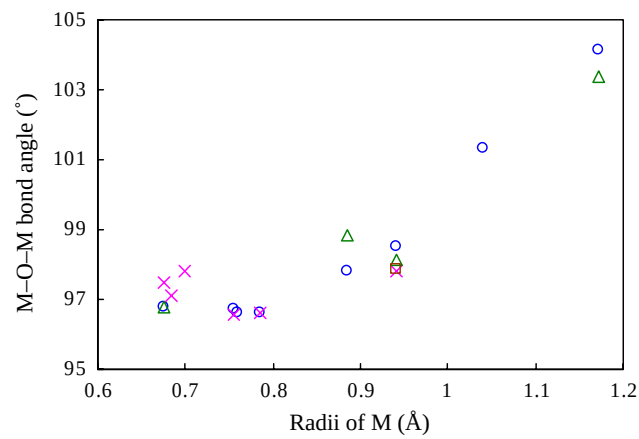

Fig. 16. Bond angles M–O–M (or O–M–O) vs. the size of M cations. Cross points, from left to right, are for $AgAlO_2$ [16], $AgCoO_2$ [17], $AgNiO_2$ [17], $AgCrO_2$ [18], $AgFeO_2$ [19,20] and $AgInO_2$ [21]. Open circles, from left to right, are for $CuAlO_2$ [9], $CuCrO_2$ [22], $CuGaO_2$ [23], $CuFeO_2$ [19,20], $CuScO_2$ [24], $CuInO_2$ [25], $CuYO_2$ [23], $CuLaO_2$ [26]. The square is for $AgInO_2$ (this work), and the triangles are for $CuMO_2$ (this work).

always intermediate between these two ideal values and tends to increase with increasing size of M (Fig. 16).

4.2. Trends with temperature

NTE behavior of the c cell edge is observed in all six compounds we examined (Fig. 3). The NTE behavior for c exists only below room temperature because with increasing temperature it is overwhelmed by the positive thermal expansion of the M–O bonds (Fig. 10). For

CuMO$_2$ compounds, the NTE behavior of c can always be attributed to the apparent NTE behavior of the Cu–O bond distance (Fig. 9). This behavior can in turn be related to the large thermal displacements of Cu perpendicular to the O–Cu–O linkage. Correction for this thermal motion generally gives Cu–O distances that increase with increasing temperature (Fig. 9). The correction used was a riding motion correction [30], which assumes that the thermal motion of the A cation is in the same direction as the thermal motion of oxygen. If this correlation were not assumed, the corrected A–O distances would increase even more with increasing temperature. We had previously suggested that the degree of NTE behavior was linked to the Cu–Cu distance [8]. As this distance becomes smaller, the transverse thermal motion of the A cation would be impeded. In fact, the smallest U_{11} values for Cu are found in CuAlO$_2$ where the Cu–Cu distance is the smallest (Fig. 5). Furthermore, the strongest low temperature NTE behavior for the apparent Cu–O distance is found in CuLaO$_2$ ($\alpha = -6.4 \times 10^{-6}$/K) compared to $\alpha = -5.9 \times 10^{-6}$/K in 3R CuScO$_2$ and $\alpha = -3.2 \times 10^{-6}$/K in CuAlO$_2$. Also, the NTE behavior for the apparent Cu–O distance has disappeared by 500 K for CuAlO$_2$ whereas it continues strong to higher temperatures in CuLaO$_2$. The NTE behavior of the corrected Cu–O distance at low temperature in CuLaO$_2$ suggests that the riding motion correction is too conservative.

There is no indication of NTE behavior for the Ag–O distance in AgInO$_2$ (Fig. 9). This might be considered surprising in view of the stronger NTE behavior of Ag$_2$O compared to that of Cu$_2$O [7]. However, the Ag–Ag distance in Ag$_2$O is 3.42 Å whereas this distance is only 3.28 Å in AgInO$_2$. Thus, the Ag thermal displacements perpendicular to O–Ag–O linkages will be inhibited in AgInO$_2$ relative to Ag$_2$O. In fact, the magnitude of the thermal motion of Ag perpendicular to the O–Ag–O linkage in Ag$_2$O is reported to be more than two times what we find in AgInO$_2$ [31,32]. Thus, although the U_{11} values for Ag in AgInO$_2$ are comparable to those of CuMO$_2$ compounds showing NTE behavior, this is not enough to compensate for the very large intrinsic thermal expansion of the Ag–O bond. Weaker bonds show higher thermal expansion than stronger bonds, and an Ag–O bond is weaker than a Cu–O bond. Thus, the high temperature thermal expansion in AgInO$_2$ for both the Ag–O distance and the c cell edge is much higher than the corresponding values for the CuMO$_2$ delafossites (Figs. 3 and 9).

For AMO$_2$ delafossites it is the decrease in the M–O distance with decreasing temperature that primarily causes the a cell edge to decrease with decreasing temperature. However, the forces between the A cations can also be expected to have some impact on the thermal expansion of the a cell edge, and Ag–Ag and Cu–Cu repulsive or attractive forces are not the same (Fig. 14). The A–A distances for these AInO$_2$ compounds lie to the right of the minima in Fig. 14. Thus, the Ag–Ag attractive forces in AgInO$_2$ are expected to be stronger than the Cu–Cu attractive forces in CuInO$_2$. On cooling, this could in turn cause a stronger contraction of the a cell edge in AgInO$_2$ than in CuInO$_2$, as observed. This greater thermal contraction with decreasing temperature of the a cell edge for AgInO$_2$ causes the slight expansion of the $(InO_2)^{1-}$ layer at lower temperatures and consequently a small NTE effect for the c-axis.

Comparisons of trends for 2H and 3R CuScO$_2$ are complicated by the fact that Mg substitution for Sc was used to stabilize the 2H form. We know that it is this substitution that causes the smaller a cell edge and the larger c cell edge for our 2H sample [11]. The effect of the smaller Mg(II) for Sc(III) is also clearly seen in the plot of M–O distances vs. temperature in Fig. 10. The larger Cu–O distance and resultant longer c cell edge for 2 H CuScO$_2$ are again more likely due to the Mg substitution than the different stacking along the c-axis.

The most surprising NTE behavior found in this study is that of the a cell edge for CuLaO$_2$ at low temperatures (Fig. 2). Data were collected at more temperatures in the low temperature range for CuLaO$_2$ to confirm with certainty the cause of this behavior. This NTE behavior is not caused by NTE behavior of the La–O distance (Fig. 10). Rather it is caused by continued shrinkage of the thickness of the $(LaO_2)^{1-}$ sheet with decreasing temperature (Fig. 11), even after the La–O distance has leveled off. The other $(MO_2)^{1-}$ sheets also show continued shrinkage down to low temperatures, but not as so strongly as for CuLaO$_2$. Furthermore, the La–O distance flattens out sooner with decreasing temperature than for the other compounds. Geometric considerations dictate that a decreasing $(LaO_2)^{1-}$ sheet thickness coupled with an invariant La–O distance will directly cause an increase in the a cell edge.

Acknowledgments

This research was supported by NSF. We also acknowledge the support of the National Institute of Standards and Technology, US Department of Commerce in providing the neutron facilities and the University of Maryland Outreach Program for partial support of this work. Certain commercial products are identified to document experimental procedures. Such identification is not intended to imply recommendation or endorsement by the National Institute of Standards and Technology, nor is it intended to imply these products are necessarily the best available for the purpose.

References

[1] A.W. Sleight, Inorg. Chem. 37 (1998) 2854–2860.
[2] D.J. Williams, D.E. Partin, F.J. Lincoln, J. Kouvetakis, M. O'Keeffe, J. Solid State Chem. 134 (1997) 164–169.
[3] G.K. White, R.B. Roberts, Aust. J. Phys. 41 (1988) 791–795.
[4] G.A. Slack, I.C. Huseby, J. Appl. Phys. 53 (1982) 6817–6822.
[5] H.A. Mook, F. Holtzberg, in: L.M. Falicov, W. Hanke, M.B. Maple (Eds.), Valence Fluctuations in Solids, North-Holland Publishing Company, Amsterdam, 1981, pp. 113–118.
[6] J.R. Salvador, F. Guo, T. Hogan, M.G. Kanatzidis, Nature 425 (2003) 702–705.
[7] W. Tiano, M. Dapiaggi, G. Artioli, J. Appl. Crystallogr. 36 (2003) 1461–1463.
[8] J. Li, A. Yokochi, T.G. Amos, A.W. Sleight, Chem. Mater. 14 (2002) 2602–2606.
[9] T. Ishiguro, N. Ishizawa, N. Mizutani, M. Kato, J. Solid State Chem. 41 (1982) 132–137.
[10] R.J. Cava, H.W. Zandbergen, A.P. Ramirez, H. Takagi, C.T. Chen, J.J. Krajewski, W.F. Peck Jr., J.V. Waszczak, G. Meigs, R.S. Roth, L.F. Schneemeyer, J. Solid State Chem. 104 (1993) 437–452.
[11] J. Li, A.F.T. Yokochi, A.W. Sleight, Solid State Sci. 6 (2004) 831–839.
[12] J.S. Kasper, K. Lonsdale (Eds.), International Tables for X-ray Crystallography, Vol. II, The Kynoch Press, Birmingham, 1959, pp. 295–297.
[13] B.H. Toby, EXPGUI, a graphical user interface for GSAS, J. Appl. Crystallogr. 34 (2001) 210–221.
[14] A.C. Larson, R.B. Von Dreele, Generalized Structure Analysis System (GSAS), LANSCE, Los Alamos National Laboratory, 2001.
[15] M. Jansen, Angew. Chem. Int. Ed. Engl. 26 (1987) 1098–1110.
[16] G. Brachtel, M. Jansen, Cryst. Struct. Commun. 10 (1981) 173–174.
[17] Y.J. Shin, J.P. Doumerc, P. Dordor, M. Pouchard, P. Hagenmuller, J. Solid State Chem. 107 (1993) 194–200.
[18] S. Angelov, J.P. Doumerc, Solid State Commun. 77 (1991) 213–214.
[19] R.D. Shannon, D.B. Rogers, C.T. Prewitt, Inorg. Chem. 10 (1971) 713–718.
[20] C.T. Prewitt, R.D. Shannon, D.B. Rogers, Inorg. Chem. 10 (1971) 719–723.
[21] B.U. Kohler, M. Jansen, J. Solid State Chem. 71 (1987) 566–569.
[22] O. Crottaz, F. Kubel, H. Schmid, J. Solid State Chem. 122 (1996) 247–250.
[23] B.U. Kohler, M. Jansen, Z. Anorg. Allg. Chem. 543 (1986) 73–80.
[24] J.P. Doumerc, A. Ammar, A. Wichainchai, M. Pouchard, P. Hagenmuller, J. Phys. Chem. Solids 48 (1987) 37–43.
[25] M. Shimode, M. Sasaki, K. Mukaida, J. Solid State Chem. 151 (2000) 16–20.
[26] V.H. Haas, E. Kordes, Z. Kristallogr. Bd. 129 (1969) S259–S270.
[27] H.C. Kandpal, R. Seshadri, Solid State Sci. 4 (2002) 1045–1052.
[28] R. Nagarajan, N. Duan, M.K. Jayaraj, J. Li, K.A. Vanaja, A. Yokochi, A. Draeseke, J. Tate, A.W. Sleight, Int. J. Inorg. Mater. 3 (2001) 265–270.
[29] M. Elazhari, A. Ammar, M. Elaatmani, M. Trari, J.P. Doumerc, Eur. J. Solid State Inorg. Chem. 34 (1997) 503–509.
[30] W.R. Busing, H.A. Levy, Acta Crystallogr. 17 (1964) 142–146.
[31] G. Artioli, Energy modeling in minerals, in: C.M. Gramaccioli (Ed.),, EMU Notes in Mineralogy, vol. 4, Budapest, 2002.
[32] S.A. Beccara, G. Dalba, P. Fornasini, R. Grisenti, A. Sanson, F. Rocca, Phys. Rev. Lett. 89 (2002) 025503(1–4).